Progress In Electromagnetics Research B, Vol. 46, 193–212, 2013

SYMMETRICAL SIX-PORT WAVEGUIDE JUNCTION WITH METALLIC POST AND DIELECTRIC SLEEVE IN OVER-SIZED CAVITY

Meysam Sabahialshoara* **and Swee Ping Yeo**

National University of Singapore, Kent Ridge, Singapore 117583, Singapore

Abstract—The Least-Squares Boundary Residual Method is employed in the present paper to develop a computer model of the symmetrical six-port waveguide junction. The analytical formulation is difficult because of the insertion of a metallic post together with a dielectric sleeve into the over-sized cavity of the junction. Computational and experimental tests confirm that the resultant model is able to compute the scattering parameters of such a structurally-complicated component with numerical accuracies of ± 0.001 and $\pm 0.1^\circ$ for magnitude and phase respectively.

1. INTRODUCTION

The building blocks of waveguide circuits are commonly based on one-, two-, three- and four-port components [1–3]. With the ever-increasing expectations imposed on modern-day circuits, however, microwave designers may nowadays have to seek recourse to novel components with five or more ports [4–6] in order to meet more complex functional requirements. In particular, various six-port components [7–13] have already been attracting the attention of researchers who utilized a diversity of numerical techniques to develop computer models for predicting their performance characteristics.

Researchers [14–27] have also found it interesting to study the family of symmetrical N-port waveguide junctions; for the generic case described by Bialkowski [14], N rectangular-waveguide arms are affixed at regular azimuthal intervals to a central circular-waveguide cavity. The most familiar of these symmetrical structures are the $N = 3$ and $N = 4$ junctions which have benefited from decades of research for use

Received 23 September 2012, Accepted 26 November 2012, Scheduled 29 November 2012

* Corresponding author: Meysam Sabahialshoara (m.sabahi@gmail.com).

as circulators [15]. In addition, the $N = 4$ junction has been proposed for switch [17], vircator [18] and crossover [19] applications. Although not as well-known, the $N = 5$ junction has been attracting interest as well [20–24]; such a component can function as a four-way power divider [20] and suitable prototypes have been designed for combining the power outputs of four Gunn diodes [21] or for directing power flow within six-port reflectometers [22]. Extending this line of study, we shall thus consider the $N = 6$ junction where its scattering matrix may in general be written in the following form (based on its six-fold rotational symmetry and network reciprocity properties):

$$\underline{S} = \begin{bmatrix} \gamma & \alpha & \beta & \tau & \beta & \alpha \\ \alpha & \gamma & \alpha & \beta & \tau & \beta \\ \beta & \alpha & \gamma & \alpha & \beta & \tau \\ \tau & \beta & \alpha & \gamma & \alpha & \beta \\ \beta & \tau & \beta & \alpha & \gamma & \alpha \\ \alpha & \beta & \tau & \beta & \alpha & \gamma \end{bmatrix}. \tag{1}$$

It is beneficial for us to draw upon the experience already gained by the researchers who successfully developed models for the symmetrical five-port waveguide junction. As depicted in Figure 1, our $N = 6$ structure incorporates various features that resemble those reported for the earlier $N = 5$ prototypes in [20–24]:

(a) According to Montgomery et al. [20], the insertion of a rotationally symmetric object (such as dielectric sleeve) together with a metallic post into the cylindrical cavity will offer us greater flexibility in adjusting the phases of the eigenvalues associated with the component's scattering matrix. Similar to the $N = 5$ junction designed by Yeo et al. [23], we have added a concentric sleeve (of relative permittivity ε_r) in Figure 1; such a dielectric-loaded cavity will support hybrid modes which have more complicated field expressions when compared with the pure TE and TM modes that can be expected inside a coaxial cavity for the simplified case of $\varepsilon_r = 1$.

(b) The simulation results obtained by Chumachenko and Zinenko [24] for their $N = 5$ junction suggest that the size of the central cavity may be appropriately enlarged in order to optimize coupling. As can be seen from the cross-sectional view of our $N = 6$ structure in Figure 1(b), we have opted instead for an over-sized cavity where its height h is longer than the broad dimension a of each rectangular-waveguide arm. The immediate consequence of allowing for $h > a$ is that a wider array of additional rectangular-waveguide TE and TM modes must be taken into account during the formulation of our junction model in Section 2.

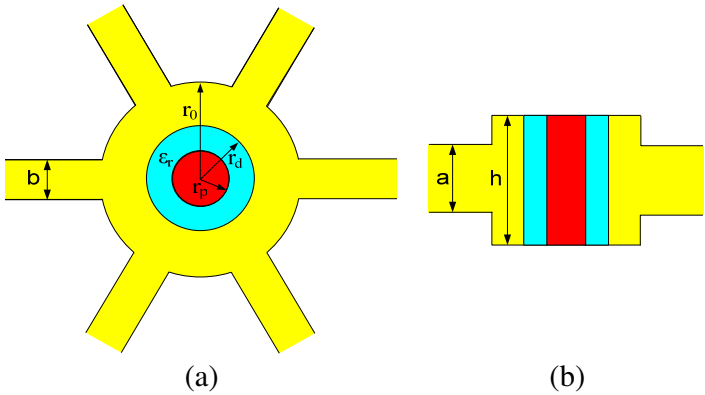

Figure 1. Symmetrical six-port waveguide junction with metallic post and dielectric sleeve in over-sized (E-plane coupled) cavity. (a) Top view, (b) mid-sectional view.

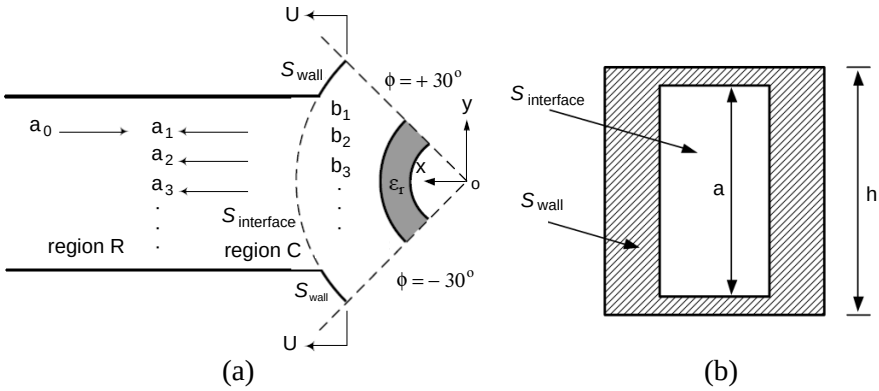

Figure 2. One-sixth segment of waveguide junction depicted in Figure 1. (a) Top view, (b) cross-sectional view U-U.

2. EIGENMODE MODEL

When developing his generic model of the symmetrical N-port waveguide junction (with its central cavity containing a metallic post without any dielectric sleeve), Bialkowski [14] chose a non-eigenmode approach and included only the simpler TE modes in his field-matching analysis. For our case, however, it is more expedient for us to capitalize on the six-fold rotational symmetry of the $N = 6$ structure shown in Figure 1(a) so as to develop an eigenmode model of the one-sixth

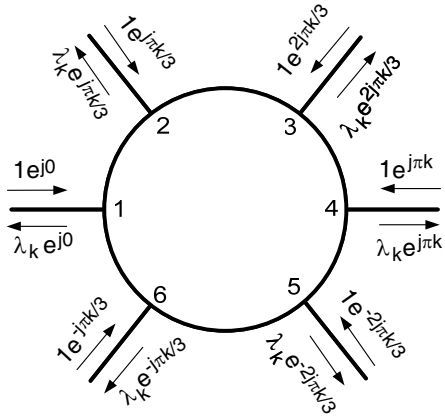

Figure 3. Schematic arrangement of input and output waves at ports of waveguide junction depicted in Figure 1 when operating in eigenmode (of order $k = 0, 1, 2, 3, 4, 5$).

segment sketched in Figure 2 (where the coordinates are defined with reference to the center O on the z-axis of the cylindrical cavity).

It is known that the symmetrical six-port junction supports a total of six eigenmodes [25]. The general arrangement of input and output waves associated with any of these eigenmodes is schematically portrayed in Figure 3; for the eigenmode of order k (where $k = 0, 1, 2, 3, 4, 5$), the input waves at the six ports have the same amplitude (which we normalize to 1) but their phases differ by $\pm jk\pi/3$ for any pair of neighboring ports. We thus have to append an additional eigenmode-related condition (*viz.* BC7) to the following list of boundary conditions that must be satisfied during our derivation of the field-matching equations:

BC1 negligible tangential electric fields over the metallic walls at $z = \pm\frac{1}{2}a$ and $y = \pm\frac{1}{2}b$ of the rectangular waveguide (denoted as Region R in Figure 2).

BC2 negligible tangential electric fields over the metallic terminations at $z = \pm\frac{1}{2}h$ of the cylindrical cavity (denoted as Region C in Figure 2).

BC3 negligible tangential electric field over the metallic surface at $r = r_p$ of the central post.

BC4 continuity of tangential electric- and magnetic-field components across the dielectric-air interface at $r = r_d$ of the concentric sleeve.

BC5 continuity of tangential electric- and magnetic-field components

across the interface (represented by $S_{\text{interface}}$ in Figure 2) between Regions R and C.

BC6 negligible tangential electric field over the metallic wall (represented by S_{wall} in Figure 2) at $r = r_0$ of the cylindrical cavity.

BC7 eigenmode-related inter-relationships for the azimuthal variation of the electric- and magnetic-field distributions in any pair of adjoining 60° sectors within the cylindrical cavity.

BC1, BC2, BC3 and BC4 have been incorporated directly into the hybrid expressions we selected to represent the modal fields within Regions R and C while BC7 in essence specifies the type of azimuthal variation allowed in Region C for any particular eigenmode. BC5 is especially difficult to implement and we need to define two error parameters that measure the residual mismatch of the respective field components tangential to $S_{\text{interface}}$:

$$\Delta_A = \iint_{S_{\text{interface}}} \left| \sum_{p=0}^{P} a_p \vec{e}_p^{\,R} - \sum_{q=1}^{Q} b_q \vec{e}_q^{\,C} \right|^2 ds \tag{2}$$

$$\Delta_B = \iint_{S_{\text{interface}}} \left| \sum_{p=0}^{P} a_p \vec{h}_p^{\,R} - \sum_{q=1}^{Q} b_q \vec{h}_q^{\,C} \right|^2 ds \tag{3}$$

where, as portrayed in Figure 2(a), the TE_{10} wave incident from the source is denoted by a_0 (which we normalize to $1 + j0$) and where $a_1, a_2, a_3, \ldots$ are the coefficients assigned to the different back-scattered modes in Region R and $b_1, b_2, b_3, \ldots$ are the coefficients assigned to the various cavity modes excited in Region C. We have reproduced in the Appendix the expressions for the electric and magnetic fields $\vec{e}_p^{\,R}$ and $\vec{h}_p^{\,R}$ associated with the pth mode in Region R as well as $\vec{e}_q^{\,C}$ and $\vec{h}_q^{\,C}$ associated with the qth mode in Region C. In addition, we need to define another field-mismatch parameter for BC6 to measure the residual electric field tangential to S_{wall}:

$$\Delta_C = \iint_{S_{\text{wall}}} \left| \sum_{q=1}^{Q} b_q \vec{e}_q^{\,C} \right|^2 ds \tag{4}$$

Given the complexity of our junction structure and the concomitant requirement for hybrid field expressions, we have opted to minimize $\Delta_{\text{sum}} = \Delta_A + \eta_0^2 \Delta_B + \Delta_C$ (where η_0 is the free-space impedance) by employing the Least Squares Boundary Residual Method (LSBRM) because this numerical technique has been found by others to be rigorous:

(i) Davies [28, p. 102] already demonstrated that "convergence to the physically correct solution is assured" for the LSBRM.

(ii) during their computational trials, Bunch et al. [29, p. 1027] observed that "boundary residual methods find the best fit to field continuity and furthermore they converge to the exact solution as the number of wave functions increased".

(iii) in his tutorial paper where he explained the mathematical differences between the LSBRM and Galerkin's method, Sarkar [30, p. 1222] agreed that "only the method of least squares guarantees the convergence of the residuals as the order of the approximation gets higher" but he also pointed out that "this advantage is, however, offset by the fact that the method of least squares requires considerably more computations".

(iv) Oraizi [31, p. 58] concluded from his literature survey that "boundary-value problems... can be readily handled by the LSBRM."

Each of the three boundary residuals defined in (2)–(4) is clearly positive semi-definite. In essence, the formulation of our LSBRM model is based on the following minimization of the positive semi-definite Δ_{sum} with respect to the unknown a_p and b_q coefficients:

$$\frac{\partial}{\partial a_p}\Delta_{\text{sum}} = 0 \quad \text{for} \quad p = 1, 2, 3, \ldots, P \tag{5}$$

$$\frac{\partial}{\partial b_q}\Delta_{\text{sum}} = 0 \quad \text{for} \quad q = 1, 2, 3, \ldots, Q. \tag{6}$$

The $P+Q$ inhomogeneous equations contained in (5), (6) may be more conveniently recast in compact matrix notation:

$$\underline{U}\underline{x} = \underline{v} \tag{7}$$

where all of the modal coefficients a_1, a_2, a_3, ..., a_P, b_1, b_2, b_3, ..., b_Q are placed sequentially in the column vector $\underline{x}$ while the various entries in the square matrix $\underline{U}$ and column vector $\underline{v}$ consist of the self- and inter-coupling integrals among the different modes of Regions R and C. The detailed expressions for these coupling integrals are available in [10] (which can be readily downloaded from the thesis archive website hosted by National University of Singapore).

Although the $N = 6$ junction has six eigenvalues λ_k (where $k = 0, 1, 2, 3, 4, 5$ is the order of the associated eigenmode), two pairs are known to be degenerate [25]. The numerical solution of the matrix equation in (7) for the unknown vector $\underline{x}$ yields all of the modal coefficients a_p (where $p = 1, 2, 3, \ldots, P$) and b_q (where

Table 1. Convergence of LSBRM-generated results for eigenvalues of junction depicted in Figure 1. ($a = 22.9\,\text{mm}$, $b = 10.2\,\text{mm}$, $h = 26.5\,\text{mm}$, $r_0 = 13.4\,\text{mm}$, $r_d = 5.0\,\text{mm}$, $r_p = 1.8\,\text{mm}$, $\varepsilon_r = 3$ and $f = 10\,\text{GHz}$).

$P = Q$	Eigenvalues (λ_k)					
	$k = 0$	$k = 1$	$k = 2$	$k = 3$	$k = 4$	$k = 5$
50	0.9031∠-24.2°	0.8807∠9.9°	0.9698∠-63.5°	0.9512∠-110.5°	0.9694∠-163.5°	0.8819∠9.8°
150	0.9714∠-21.3°	0.9693∠11.6°	0.9869∠-163.0°	0.9780∠-108.1°	0.9869∠-163.0°	0.9693∠11.6°
250	0.9793∠-20.7°	0.9788∠12.0°	0.9908∠-162.8°	0.9834∠-107.5°	0.9908∠-162.8°	0.9788∠12.0°
350	0.9817∠-20.5°	0.9815∠12.2°	0.9922∠-162.6°	0.9852∠-107.1°	0.9922∠-162.6°	0.9815∠12.2°
500	0.9833∠-20.1°	0.9834∠12.4°	0.9931∠-162.4°	0.9868∠-106.8°	0.9931∠-162.4°	0.9834∠12.4°
650	0.9877∠-19.8°	0.9877∠12.6°	0.9949∠-162.2°	0.9903∠-106.5°	0.9949∠-162.2°	0.9876∠12.6°
800	0.9899∠-19.6°	0.9897∠12.8°	0.9956∠-162.1°	0.9918∠-106.3°	0.9956∠-162.1°	0.9897∠12.8°
950	0.9906∠-19.6°	0.9905∠12.8°	0.9960∠-162.1°	0.9925∠-106.2°	0.9960∠-162.1°	0.9905∠12.8°

$q = 1, 2, 3, \ldots, Q$) for each eigenmode and the four non-degenerate eigenvalues are then computed via the following relationship:

$$\lambda_k = \left(\frac{a_1}{a_0}\right)_k \quad \text{for} \quad k = 0, 1, 2, 3. \tag{8}$$

For the remaining two eigenvalues, we infer from the junction's six-fold rotational symmetry that $\lambda_4 = \lambda_2$ and $\lambda_5 = \lambda_1$ [25] as can also be seen from the sample results presented in Table 1 (as well as all of the other numerical results we have compiled in [10]) even when our LSBRM model employs only 50 modes during the numerical computations.

Since both metal and dielectric have been presumed to be loss-free for the symmetrical six-port waveguide junction shown in Figure 1, $\underline{S}$ in (1) must be a unitary matrix and the eigenvalues generated by our computer model ought to have unit magnitudes. It is evident from the numerical results of Table 1 that all eigenvalue magnitudes $|\lambda_k|$ do converge monotonically towards 1 as we increase the number of modes P and Q used to represent the fields in Regions R and C respectively. In view of this, what we should retain for our ensuing computations are the numerical results for the eigenvalue phases θ_k which correspondingly converge in Table 1 to within $\pm 0.1°$ when P and Q exceed 800 for all six eigenmodes. Given the level of accuracy obtainable by our LSBRM model for θ_k, we can confidently proceed to compute the various scattering parameters defined in (1) via the following equations [10] (which are derived via the superposition of the output waves portrayed in Figure 3 for all possible eigenmodes [25]):

$$\alpha = \frac{1}{6}\left\{e^{j\theta_0} + e^{j\theta_1} - e^{j\theta_2} - e^{j\theta_3}\right\} \tag{9}$$

$$\beta = \frac{1}{6}\left\{e^{j\theta_0} - e^{j\theta_1} - e^{j\theta_2} + e^{j\theta_3}\right\} \tag{10}$$

$$\gamma = \frac{1}{6}\left\{e^{j\theta_0} + 2e^{j\theta_1} + 2e^{j\theta_2} + e^{j\theta_3}\right\} \tag{11}$$

$$\tau = \frac{1}{6}\left\{e^{j\theta_0} - 2e^{j\theta_1} + 2e^{j\theta_2} - e^{j\theta_3}\right\} \tag{12}$$

3. TEST RESULTS

Table 2 presents a sample of the numerical results we obtained via (9)–(12) for the scattering parameters of the symmetrical six-port waveguide junction depicted in Figure 1. Since we have allowed for an over-sized cavity with $h > a$, we need to include both TE_{mn} and TM_{mn} modes (where $m = 1, 3, 5, \ldots$ and $n = 1, 2, 3, \ldots$) to represent the rectangular-waveguide fields in Region R as well as hybrid modes to describe the dielectric-loaded cavity fields in Region C. Hence, it is not surprising to find in Tables 1 and 2 that our LSBRM model requires a large number of modes (with P and Q exceeding 800) before the computed results for α, β, γ, τ and λ_k converge to ± 0.001 and $\pm 0.1^\circ$ for magnitude and phase respectively.

We have, for convenience, opted for the default choice of $P = Q$ during the computations. In view of Davies' assertion that "the least-squares approach avoids problems of relative convergence" [28, p. 100] (which are known to affect certain numerical techniques as explained in [32]), our LSBRM-based model should allow other $\frac{P}{Q}$ ratios to be adopted as well. To dispel any possibility of concern (as alluded

Table 2. Convergence of LSBRM-generated results for scattering parameters of junction depicted in Figure 1. ($a = 22.9\,\mathrm{mm}$, $b = 10.2\,\mathrm{mm}$, $h = 26.5\,\mathrm{mm}$, $r_0 = 13.4\,\mathrm{mm}$, $r_d = 5.0\,\mathrm{mm}$, $r_p = 1.8\,\mathrm{mm}$, $\varepsilon_r = 3$ and $f = 10\,\mathrm{GHz}$).
(a) Using default choice of $P = Q$.

# modes	Scattering parameters computed with different P and Q			
	α	β	γ	τ
$P = Q = 50$	0.518 ∠51.8°	0.270 ∠-48.9°	0.164 ∠-73.2°	0.442 ∠-107.1°
$P = Q = 150$	0.537 ∠52.7°	0.280 ∠-47.8°	0.160 ∠-63.9°	0.445 ∠-106.5°
$P = Q = 250$	0.540 ∠53.0°	0.280 ∠-47.4°	0.161 ∠-62.9°	0.457 ∠-106.3°
$P = Q = 350$	0.541 ∠53.1°	0.281 ∠-47.3°	0.161 ∠-62.7°	0.457 ∠-106.2°
$P = Q = 500$	0.542 ∠53.3°	0.281 ∠-47.2°	0.162 ∠-62.5°	0.457 ∠-106.1°
$P = Q = 650$	0.543 ∠53.5°	0.281 ∠-46.7°	0.164 ∠-61.6°	0.458 ∠-106.0°
$P = Q = 800$	0.544 ∠53.6°	0.281 ∠-46.5°	0.165 ∠-61.1°	0.458 ∠-105.9°
$P = Q = 950$	0.545 ∠53.7°	0.281 ∠-46.5°	0.165 ∠-61.1°	0.458 ∠-105.9°

(b) using mode ratio of $\frac{P}{Q} \approx \frac{a}{h}$.

# modes	Scattering parameters computed with different P and Q			
	α	β	γ	τ
$P = 50$, $Q = 58$	0.518 ∠51.9°	0.271 ∠-48.8°	0.165 ∠-73.0°	0.442 ∠-107.1°
$P = 150$, $Q = 174$	0.537 ∠52.8°	0.280 ∠-47.8°	0.160 ∠-63.8°	0.455 ∠-106.5°
$P = 250$, $Q = 290$	0.540 ∠53.0°	0.281 ∠-47.4°	0.161 ∠-62.9°	0.457 ∠-106.3°
$P = 350$, $Q = 406$	0.541 ∠53.2°	0.281 ∠-47.2°	0.162 ∠-62.7°	0.457 ∠-106.2°
$P = 500$, $Q = 580$	0.542 ∠53.4°	0.281 ∠-47.0°	0.163 ∠-62.1°	0.457 ∠-106.1°
$P = 650$, $Q = 752$	0.544 ∠53.6°	0.281 ∠-46.6°	0.164 ∠-61.3°	0.458 ∠-105.9°
$P = 800$, $Q = 926$	0.545 ∠53.7°	0.281 ∠-46.5°	0.165 ∠-61.1°	0.458 ∠-105.9°
$P = 950$, $Q = 1100$	0.545 ∠53.8°	0.281 ∠-46.4°	0.165 ∠-60.9°	0.458 ∠-105.8°

(c) Using mode ratio of $\frac{Q}{P} \approx \frac{\pi r_0}{3b}$.

# modes	Scattering parameters computed with different P and Q			
	α	β	γ	τ
$P = 50$, $Q = 70$	$0.531\angle 52.2°$	$0.277\angle -48.3°$	$0.157\angle -66.5°$	$0.442\angle -106.7°$
$P = 150$, $Q = 208$	$0.539\angle 52.8°$	$0.280\angle -47.7°$	$0.159\angle -63.4°$	$0.455\angle -106.4°$
$P = 250$, $Q = 346$	$0.540\angle 53.0°$	$0.281\angle -47.5°$	$0.161\angle -62.9°$	$0.457\angle -106.3°$
$P = 350$, $Q = 484$	$0.541\angle 53.2°$	$0.281\angle -47.3°$	$0.161\angle -62.7°$	$0.457\angle -106.2°$
$P = 500$, $Q = 692$	$0.543\angle 53.5°$	$0.281\angle -46.8°$	$0.163\angle -61.7°$	$0.457\angle -106.0°$
$P = 650$, $Q = 898$	$0.544\angle 53.7°$	$0.281\angle -46.5°$	$0.165\angle -61.1°$	$0.458\angle -105.9°$
$P = 800$, $Q = 1102$	$0.545\angle 53.8°$	$0.281\angle -46.4°$	$0.165\angle -60.9°$	$0.458\angle -105.8°$
$P = 950$, $Q = 1312$	$0.545\angle 53.9°$	$0.281\angle -46.2°$	$0.166\angle -60.6°$	$0.458\angle -105.8°$

in [31, 33]), we have taken additional efforts to repeat the computations when $P \neq Q$; for example, the extra sets of numerical results we recorded in [10] for different mode-ratio selections (*viz.* $\frac{P}{Q} = \frac{1}{3}, \frac{1}{2}$, 2, and 3) show no indication of relative convergence. We have also been advised to perform these computational experiments for $\frac{P}{Q} \approx \frac{a}{h}$ and $\frac{Q}{P} \approx \frac{2\pi r_0}{6b}$; the data presented in Tables 2(b) and 2(c) for these two special cases likewise confirm that the converged values for the four scattering parameters do not depend on the choice of mode ratio.

Another useful advantage of the LSBRM is that we can check the level of residual field-mismatch via the parameters Δ_A, Δ_B and Δ_C defined in (2)–(4) as stipulated by BC5 and BC6. If P and Q are allowed to be infinitely large, our LSBRM model should in the ideal case return zero values for these three field-mismatch parameters. In practice, however, there are constraints on the number of modes to be included during the actual computations. Nevertheless, we observe that the total field-mismatch level Δ_{sum} monotonically decreases towards zero in Table 3 as we steadily increase P and Q even when we have opted for different mode ratios (*viz.* $\frac{P}{Q} = \frac{1}{3}, \frac{1}{2}$, 1, 2 and 3). For ease of relative comparison, we have conveniently normalized $\Delta_{\text{sum}} = 1$ when $M = 1$ for all five columns of field-mismatch data in Table 3.

Table 3 must be supplemented by electric- and magnetic-field plots in order for us to gain some appreciation of the residual field-mismatch level associated with the numerical results for Δ_{sum}. Reproduced in Figure 4 is a sample set of field distributions at the interface $r = r_0$ between Regions R and C where we varied the linear coordinate z along the horizontal axis of the plots. Figure 5 presents another set

Table 3. Residual field-mismatch results of LSBRM-based model for junction depicted in Figure 1. ($a = 22.9\,\text{mm}$, $b = 10.2\,\text{mm}$, $h = 26.5\,\text{mm}$, $r_0 = 13.4\,\text{mm}$, $r_d = 5.0\,\text{mm}$, $r_p = 1.8\,\text{mm}$, $\varepsilon_r = 3$ and $f = 10\,\text{GHz}$).

M (number of modes)	Field-mismatch level Δ_{sum} for different P and Q				
	P=M Q=M	$P = 2M$ $Q = M$	$P = 3M$ $Q = M$	$P = M$ $Q = 2M$	$P = M$ $Q = 3M$
25	0.063	0.059	0.049	0.033	0.033
75	0.016	0.021	0.019	0.013	0.013
150	0.0094	0.012	0.011	0.0083	0.0061
300	0.0084	0.0079	0.0072	0.0054	0.0048
450	0.0052	0.0071	0.0065	0.0041	0.0039
600	0.0048	0.0060	0.0057	0.0037	0.0035

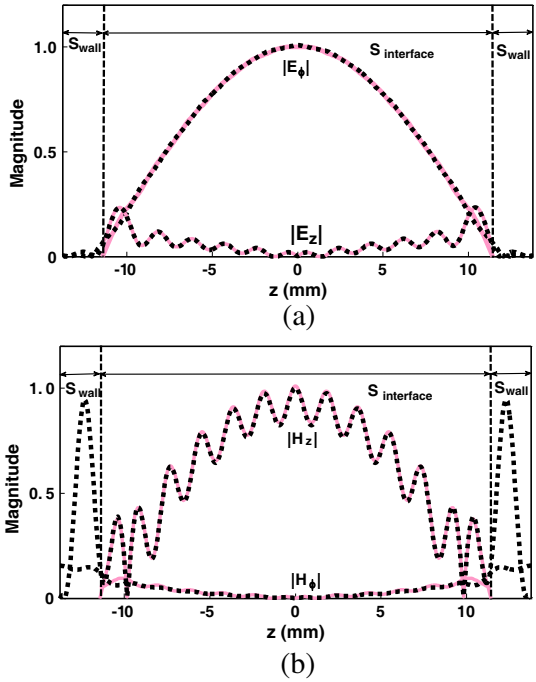

Figure 4. LSBRM-generated plots showing how electric- and magnetic-field components in Region R ($\cdots\cdots$) and Region C (—) vary along z-direction over $S_{\text{interface}}$ and S_{wall} interface for 60° sector of symmetrical six-port waveguide junction depicted in Figure 2 (where $a = 22.9\,\text{mm}$, $b = 10.2\,\text{mm}$, $h = 27.5\,\text{mm}$, $r_0 = 13.4\,\text{mm}$, $r_d = 5.0\,\text{mm}$, $r_p = 1.8\,\text{mm}$, $\varepsilon_r = 3$, $f = 10\,\text{GHz}$ and $P = Q = 950$). (a) Electric-field patterns, (b) magnetic-field patterns.

of field distributions over $S_{\text{interface}}$ and S_{wall} but this time we varied the azimuthal coordinate ϕ along the horizontal axis of the plots. The electric-field plots in Figures 4(a) and 5(a) confirm that there is excellent field-match over $S_{\text{interface}}$ (as specified by BC5) and the magnitude of the tangential electric field remains negligible over S_{wall} (as specified by BC6). In Figures 4(b) and 5(b), our implementation of BC5 over $S_{\text{interface}}$ has likewise resulted in excellent matching between the magnetic fields in Regions R and C (while BC6 does not impose any corresponding requirement for the tangential magnetic field to vanish over S_{wall}).

To study the effects of the dielectric sleeve, we have additionally plotted the electric-field variation as a function of the radial coordinate

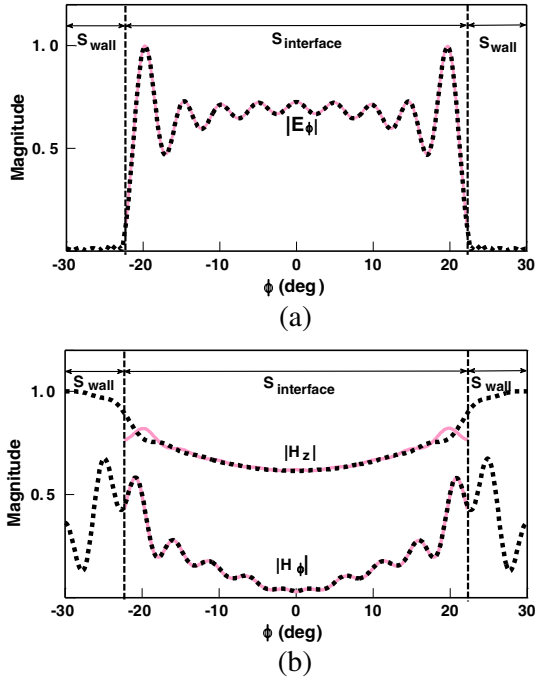

Figure 5. LSBRM-generated plots showing how electric- and magnetic-field components in Region R ($\cdots\cdots$) and Region C (—) vary along φ-direction over $S_{\text{interface}}$ and S_{wall} interface for 60° sector of symmetrical six-port waveguide junction depicted in Figure 2 (where $a = 22.9\,\text{mm}$, $b = 10.2\,\text{mm}$, $h = 27.5\,\text{mm}$, $r_0 = 13.4\,\text{mm}$,$r_d = 5.0\,\text{mm}$, $r_p = 1.8\,\text{mm}$, $\varepsilon_r = 3$, $f = 10\,\text{GHz}$ and $P = Q = 950$). (a) Electric-field patterns, (b) magnetic-field patterns.

r in Figure 6 (where the field continuity observed at $r = r_d$ and $r = r_0$ provides further affirmation that the boundary conditions at these interfaces have been adequately met). For Bialkowski's model [14], there is no need for hybrid modes to be taken into account because his central cavity does not contain any dielectric. For our dielectric-loaded structure, we note from Figure 6(b) that $|E_z|$ decreases towards zero when ε_r is reduced from 6 to 1.1. In any event, $|E_z|$ must decay with increasing r for all plots in Figure 6(b) because each of the electric-field patterns will have to revert to that of the rectangular-waveguide TE_{10} mode when we increase r beyond r_0 into Region R. Furthermore, Figure 6(a) shows the electric fields within Region C becoming progressively concentrated in the dielectric sleeve as ε_r is increased from 1.1 to 6.

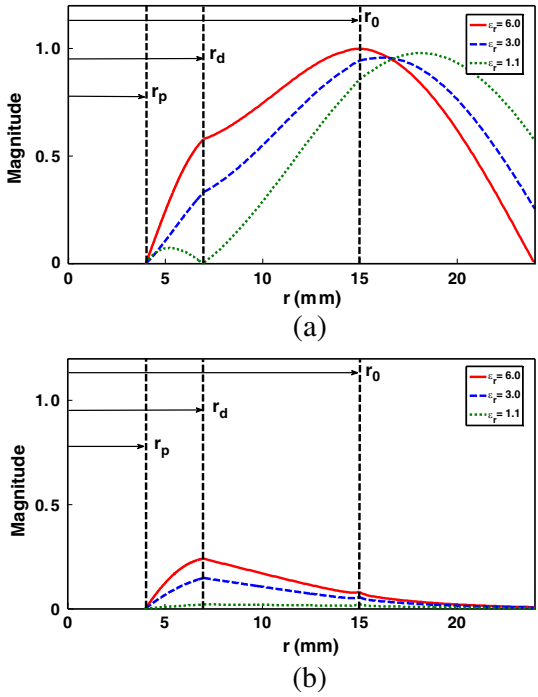

Figure 6. LSBRM-generated plots showing how electric-field components vary along r-direction for dielectric sleeve with different relative permittivity settings ($\varepsilon_r = 1.1$, 3 and 6) inside 60° sector of symmetrical six-port waveguide junction depicted in Figure 2 (where $a = 22.9\,\text{mm}$, $b = 10.2\,\text{mm}$, $h = 27.5\,\text{mm}$, $r_0 = 15.0\,\text{mm}$, $r_d = 7.0\,\text{mm}$, $r_p = 4.0\,\text{mm}$, $f = 10\,\text{GHz}$ and $P = Q = 950$, $\phi = 0°$). (a) Azimuthal electric field component e_ϕ, (b) axial electric field component e_z.

It is also useful for us to know how the junction's dimensions affect α, β, γ and τ. By way of example, we have varied in Figure 7 the central post's radius r_p over its range of permissible values from 0 to r_c (where we have opted for the convenient setting of $\varepsilon_r = 1$ so as to remove the presence of the dielectric sleeve for this particular set of computations). Such simulations offer useful insights as we can infer from the compilation of the resulting plots the appropriate range of values over which each of the junction's dimensions ought to be varied for design purposes; returning to our example in Figure 7, we accordingly learn that r_p should not be allowed to be too large as otherwise the metallic post dominates the interior of the cavity and effectively becomes a short-circuit termination at the $r_p = r_0$ limit.

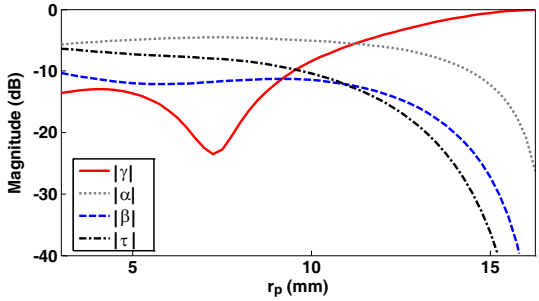

Figure 7. LSBRM-generated plots showing how scattering parameters vary with metallic-post radius for junction depicted in Figure 1 (where $a = 22.9\,\text{mm}$, $b = 10.2\,\text{mm}$, $h = 27.5\,\text{mm}$, $r_0 = 16.5\,\text{mm}$, $\varepsilon_r = 1$, $f = 10\,\text{GHz}$ and $P = Q = 950$).

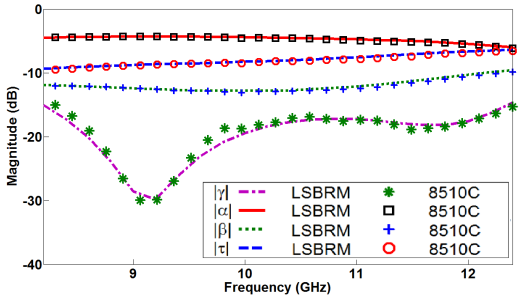

Figure 8. Comparison of LSBRM-generated plots and 8510C-measured results for scattering parameters of prototype depicted in Figure 1 (where $a = 22.9\,\text{mm}$, $b = 10.2\,\text{mm}$, $h = 25.8\,\text{mm}$, $r_0 = 14.2\,\text{mm}$, $r_d = 6.7\,\text{mm}$, $r_p = 4.8\,\text{mm}$ and $\varepsilon_r = 2.1$).

The test results we presented thus far have been obtained from computational simulations. There is also a need for comparison with experimental results so as to check the validity of the assumptions incorporated during our analytical formulation. We have therefore fabricated a prototype with over-sized cavity and six WR90 arms (based on the structure schematically reproduced in Figure 1) and measured its scattering parameters by using the 8510C vector network analyzer available in our laboratory. The close agreement between the predicted and measured results plotted in Figure 8 for α, β, γ and τ over the frequency range from 8.2 GHz to 12.4 GHz provides further corroboration that the numerical results generated by our LSBRM model are accurate and reliable for use in computer-aided design.

4. CONCLUSION

We have demonstrated in the present paper that the structurally complicated junction depicted in Figure 1 is amenable to rigorous analysis. The non-eigenmode analysis employed by Bialkowski [14] appears simpler but it should be remembered that there is no dielectric sleeve inside his central cavity which, furthermore, is not over-sized. We have chosen to utilize the LSBRM because of the need to generate reliable results that are free from any possibility of spurious solutions. The various tests we performed in Section 3 have confirmed that our computer model is capable of yielding accuracies of ± 0.001 for magnitude and $\pm 0.1^\circ$ for phase with no evidence of relative convergence in the numerical results for the junction's eigenvalues and scattering parameters. Another helpful feature (not available in Bialkowski's model) is that we can readily ascertain the level of residual field-mismatch by simply computing the error parameter Δ_{sum} defined via (2)–(4) as part of our LSBRM formulation.

As pointed out in Sarkar's tutorial paper [30] which compared the method of least squares with Galerkin's method, our LSBRM model requires significantly more computational resources. Fortunately, access to powerful computing facilities is readily available nowadays and the LSBRM's number-crunching requirements have not posed any major obstacles during our series of validation tests. The resultant model is thus suitable for use with optimization routines in the computer-aided design of symmetrical six-port waveguide junctions (such as the one we recently attempted in [27]).

APPENDIX.

The boundary residuals defined in (2)–(4) are based on the modal field components that are tangential to $S_{\text{interface}}$ and S_{wall}. Reproduced in (A1)–(A4) are the tangential-field expressions where BC1 has been incorporated for the TE_{mn} and TM_{mn} modes in Region R. Since the incident a_0 wave is propagating in the dominant TE_{10} mode, we infer from symmetry about the mid-plane $z = 0$ that the mode indices required for the back-scattered waves a_1, a_2, a_3, ... included in (2)–(4) are $m = 1, 3, 5, \ldots$ and $n = 1, 2, 3, \ldots$ respectively.

$$e_\phi^R = \Big\{\Big[j\omega\mu_0\Big(\frac{m\pi}{a}\Big)H_{mn}^R + \alpha_{mn}\Big(\frac{n\pi}{b}\Big)E_{mn}^R\Big]\cos\phi\cos\Big(\frac{n\pi}{b}g(\phi)\Big) + k_{Rmn}^2\sin\phi\sin\Big(\frac{n\pi}{b}g(\phi)\Big)E_{mn}^R\Big\}\sin\Big[\frac{m\pi}{a}\Big(z+\frac{a}{2}\Big)\Big]\exp(\alpha_{mn}f(\phi)) \quad (13)$$

$$e_z^R = \left[-j\omega\mu_0\left(\frac{n\pi}{b}\right)H_{mn}^R + \alpha_{mn}\left(\frac{m\pi}{a}\right)E_{mn}^R\right]\sin\left(\frac{n\pi}{b}g\left(\phi\right)\right) \cos\left[\frac{m\pi}{a}\left(z+\frac{a}{2}\right)\right]\exp\left(\alpha_{mn}f(\phi)\right) \tag{14}$$

$$h_\phi^R = \left\{\left[-j\omega\varepsilon_0\left(\frac{m\pi}{a}\right)E_{mn}^R + \alpha_{mn}\left(\frac{n\pi}{b}\right)H_{mn}^R\right]\cos\phi\sin\left(\frac{n\pi}{b}g(\phi)\right) - k_{Rmn}^2\sin\phi\cos\left(\frac{n\pi}{b}g(\phi)\right)H_{mn}^R\right\}\cos\left[\frac{m\pi}{a}\left(z+\frac{a}{2}\right)\right]\exp(\alpha_{mn}f(\phi)) \tag{15}$$

$$h_z^R = \left[j\omega\varepsilon_0\left(\frac{n\pi}{b}\right)E_{mn}^R + \alpha_{mn}\left(\frac{m\pi}{a}\right)H_{mn}^R\right]\cos\left(\frac{n\pi}{b}g\left(\phi\right)\right) \sin\left[\frac{m\pi}{a}\left(z+\frac{a}{2}\right)\right]\exp\left(\alpha_{mn}f\left(\phi\right)\right) \tag{16}$$

where $E_{mn}^R = 0$ for TE_{mn} modes, $H_{mn}^R = 0$ for TM_{mn} modes, and

$$f\left(\phi\right) = r_0\left(1-\cos\phi\right) \tag{17}$$

$$g\left(\phi\right) = r_0\sin\phi + \frac{b}{2} \tag{18}$$

$$\left.\begin{aligned}\alpha_{mn}^2 &= \left(\frac{m\pi}{a}\right)^2 + \left(\frac{n\pi}{b}\right)^2 - \omega^2\varepsilon_0\mu_0\\ k_{Rmn}^2 &= \left(\frac{m\pi}{a}\right)^2 + \left(\frac{n\pi}{b}\right)^2\end{aligned}\right\} \begin{array}{l} m = 1,3,5,\ldots\\ n = 0,1,2,3,\ldots\end{array} \tag{19}$$

In the case of the dominant TE_{10} mode (which is the only propagating mode within Region R), the attenuation constant in (A7) is imaginary for the incident and reflected waves (represented by a_0 and a_1 respectively):

$$\begin{aligned}\alpha_{10}^{+} &= -\left|\alpha_{mn}\right|_{\substack{m=1\\n=0}} = -j\sqrt{k^2-\left(\frac{\pi}{a}\right)^2} \quad \text{for incident guided wave}\\ \alpha_{10}^{-} &= \left|\alpha_{mn}\right|_{\substack{m=1\\n=0}} = j\sqrt{k^2-\left(\frac{\pi}{a}\right)^2} \quad \text{for reflected guided wave}\end{aligned} \tag{20}$$

where $k = \omega\sqrt{\varepsilon_0\mu_0}$.

Also required for the boundary residuals defined in (2)–(4) are the following tangential-field expressions where BC2, BC3 and BC4 have been incorporated for the hybrid modes in Region C.

$$e_\phi^C = j\left\{\begin{array}{l}\left[-\left(\frac{m\pi}{h}\right)\left(\frac{n}{r}\right)\left(\xi_n(\beta_m r) + B_{2mn}\chi_n(\beta_m r)\right)\right.\\ \left. + \omega\mu_0\beta_m D_{1mn}\chi_n'(\beta_m r)\right]E_{mn}^C\\ + \left[-\left(\frac{m\pi}{h}\right)\left(\frac{n}{r}\right)B_{1mn}\chi_n\left(\beta_m r\right)\right.\\ \left. + \omega\mu_0\beta_m\left(\xi_n'\left(\beta_m r\right) + D_{2mn}\chi_n'(\beta_m r)\right)\right]H_{mn}^C\end{array}\right\}$$

$$\times \sin\left[\frac{m\pi}{h}\left(z+\frac{h}{2}\right)\right]\exp(jn\phi) \tag{21}$$

$$e_z^C = k_m^2\Big\{\left[\xi_n(\beta_m r)+B_{2mn}\chi_n(\beta_m r)\right]E_{mn}^C + B_{1mn}\chi_n(\beta_m r)H_{mn}^C\Big\} \times \cos\left[\frac{m\pi}{h}\left(z+\frac{h}{2}\right)\right]\exp(jn\phi) \tag{22}$$

$$h_\phi^C = j\left\{\begin{array}{l}\left[\left(\frac{m\pi}{h}\right)\left(\frac{n}{r}\right)\left(\xi_n(\beta_m r)+D_{2mn}\chi_n(\beta_m r)\right)\right. \\ \left.-\omega\varepsilon_0\beta_m B_{1mn}\chi_n'(\beta_m r)\right]H_{mn}^C \\ +\left[\left(\frac{m\pi}{h}\right)\left(\frac{n}{r}\right)D_{1mn}\chi_n(\beta_m r)\right. \\ \left.-\omega\varepsilon_0\beta_m\left(\xi_n'(\beta_m r)+B_{2mn}\chi_n'(\beta_m r)\right)\right]E_{mn}^C\end{array}\right\} \times \cos\left[\frac{m\pi}{h}\left(z+\frac{h}{2}\right)\right]\exp\left(jn\phi\right) \tag{23}$$

$$h_z^C = k_m^2\Big\{\left[\xi_n(\beta_m r)+D_{2mn}\chi_n(\beta_m r)\right]H_{mn}^C + D_{1mn}\chi_n(\beta_m r)E_{mn}^C\Big\} \times \sin\left[\frac{m\pi}{h}\left(z+\frac{h}{2}\right)\right]\exp(jn\phi) \tag{24}$$

where $H_{mn}^C = 0$ for E-type components, $E_{mn}^C = 0$ for H-type components, and

$$k_m = \sqrt{\omega^2\varepsilon_0\mu_0 - \left(\frac{m\pi}{h}\right)^2} \tag{25}$$

$$\beta_m = |k_m| \tag{26}$$

where $m = 1, 3, 5, \ldots$ and n can be obtained based on BC7. The functions $\xi_n(\beta_m r)$ and $\chi_n(\beta_m r)$ denote Bessel functions (or modified Bessel functions) of the first and second kinds respectively:

$$\xi_n(\beta_m r) = \begin{cases} J_n(\beta_m r) & k_m^2 \geq 0 \\ I_n(\beta_m r) & k_m^2 < 0 \end{cases} \tag{27}$$

$$\chi_n(\beta_m r) = \begin{cases} Y_n(\beta_m r) & k_m^2 \geq 0 \\ K_n(\beta_m r) & k_m^2 < 0 \end{cases} \tag{28}$$

The coefficients B_{1mn}, B_{2mn}, D_{1mn} and D_{2mn} in (A9)–(A12) are obtained via BC3 and BC4. In addition, BC7 stipulates that the fields within any pair of adjacent sectors in Region C are related via the following equations for any eigenmode (of order $k = 0, 1, 2, 3, 4, 5$):

$$\vec{e}^{\,C}\left(\phi \pm \frac{\pi}{3}\right) = \vec{e}^{\,C}(\phi)\exp\left(\pm k\frac{\pi}{3}\right)$$

$$\vec{h}^{C}\left(\phi \pm \frac{\pi}{3}\right) = \vec{h}^{C}(\phi)\exp\left(\pm k\frac{\pi}{3}\right)$$

REFERENCES

1. Marcuvitz, N., *Waveguide Handbook*, McGraw-Hill, New York, 1951.
2. Rebollar, J. M., J. Esteban, and J. E. Page, "Full-wave analysis of three and four-port rectangular waveguide junctions," *IEEE Transactions on Microwave Theory & Techniques*, Vol. 42, 256–263, 1994.
3. Bogdanov, F. G., G. S. Kevanishvilli, G. V. Kekelia, and S. L. Prosvirni, "Analysis and design of cruciform waveguide junction with a conducting diaphragm and a dielectric layer in the main arm," *Progress In Electromagnetics Research B*, Vol. 29, 139–155, 2011.
4. San-Blass, A.-A., F. J. Perez, J. Gil, F. Mira, V. E. Boria, and B. Gimeno, "Full-wave analysis and design of broad-band turnstile junctions," *Progress In Electromagnetics Research Letters*, Vol. 24, 149–158, 2011.
5. Mansour, R. R. and R. H. Macphie, "Scattering at an N-furcated parallel-plate waveguide junction," *IEEE Transactions on Microwave Theory & Techniques*, Vol. 33, 830–835, 1985.
6. Rozzi, T., A. Morini, G. Venanzoni, and M. Farina, "Full-wave analysis of N-way power dividers by eigenvalue decomposition," *IEEE Transactions on Microwave Theory & Techniques*, Vol. 57, 1156–1162, 2009.
7. Khaddaj Mallat, N., E. Moldovan, and S. O. Tatu, "V-band quadrature phase-shift keying demodulator using WR-12 six-port," *Progress In Electromagnetics Research Letters*, Vol. 6, 193–199, 2009.
8. Alessandri, F., M. Giordano, M. Guglielmi, G. Martirano, and F. Vitulli, "A new multi-tuned six-port Riblet-type directional coupler in rectangular waveguide," *IEEE Transactions on Microwave Theory & Techniques*, Vol. 51, 1441–1448, 2003.
9. Gentili, G. G., R. Nesti, and G. Pelosi, "Analysis of six-port mode launchers for circular-waveguide corrugated-horn applications," *Microwave & Optical Technology Letters*, Vol. 17, 337–339, 1998.
10. Sabahialshoara, M., "Modeling and design of symmetrical six-port waveguide junction for six-port reflectometer application," Ph.D. Thesis, National University of Singapore, 2012, (copy available at http://scholarbank.nus.edu/handle/10635/34335).

11. Boria, V. E., S. Cogollos, H. Esteban, M. Guglielmi, and B. Gimeno, "Efficient analysis of a cubic junction of rectangular waveguides using admittance-matrix representation," *IEE Proceedings on Microwaves, Antennas & Propagation*, Vol. 147, 417–422, 2000.
12. Wessel, W., T. Sieverding, and F. Arndt, "Mode-matching analysis of general waveguide multi-port junctions," *IEEE International Microwave Symposium*, 1273–1276, 1999.
13. Wan, X. and Y. Liu, "Analysis and GA-based CAD techniques for multi-port branch-line couplers," *International Conference on Microwave & Millimeterwave Technology*, 717–720, 2002.
14. Bialkowski, M. E., "Analysis of an N-port consisting of a radial cavity and E-plane coupled rectangular waveguides," *IEEE Transactions on Microwave Theory & Techniques*, Vol. 40, 1840–1843, 1992.
15. Helszajn, J., *Waveguide Junction Circulators — Theory and Practice*, Wiley, Chichester, 1998.
16. Toda, K., I. Ohta, and M. Kishihara, "H-plane crossed-waveguide hybrids," *European Microwave Conference*, 987–990, 2006.
17. Polewski, M. and J. Mazur, "Cylindrical obstacles in multi-port waveguide junctions," *International Conference on Microwaves, Radar & Wireless Communications*, 455–458, 2002.
18. Yu, G., W. Wang, and S. Liu, "Study of cylindrical cavity used for frequency- or phase-locking vircators," *SPIE Proceedings*, Vol. 3158, 113–118, 1997.
19. Chang, K., M. Li, K. A. Hummer, and R.A. Speciale, "Low-loss waveguide four-port crossover circuit and its application for cross-slot antenna feed," *Electronics Letters*, Vol. 27, 997–998, 1991.
20. Montgomery, C. G., R. H. Dicke, and E. M. Purcell, *Principles of Microwave Circuits*, McGraw-Hill, New York, 1948.
21. Chang, K., M. Li, K. A. Hummer, and R. A. Speciale, "High-power four-way power divider/combiner," *IEEE International Microwave Symposium*, 1329–1332, 1990.
22. Bannister, D. J., J. P. Ide, and M. Perkins, "Improved six-port reflectometer based on symmetrical five-port junction," *Electronics Letters*, Vol. 28, 406–408, 1992.
23. Yeo, S. P. and L. Qiao, "Symmetrical five-port waveguide junction with -20 dB residual mismatch over waveguide bandwidth," *IEE Proceedings on Microwaves, Antennas & Propagation*, Vol. 141, 101–106, 1994.
24. Chumachenko, V. P. and I. I. Zinenko, "Matching of E-plane waveguide five-port with polygonal junction cavity," *International*

Symposium Millimeter & Sub-Millimeter Waves, 702–704, 2004.

25. Riblet, G. P. and E. R. B. Hansson, "Properties of matched symmetrical six-port waveguide junction," *IEEE Transactions on Microwave Theory & Techniques*, Vol. 32, 164–171, 1984.
26. Sabahialshoara, M., J. L. Shi, and S. P. Yeo, "Using equivalent-admittance approach to match symmetrical six-port waveguide junction," *Asia-Pacific Microwave Conference*, 1493–1496, 2009.
27. Sabahialshoara, M. and S. P. Yeo, "Designing a symmetrical six-port waveguide junction," *International Microwave Symposium*, 2011, DOI:10.1109/MWSYM.2011.5972620.
28. Davies, J. B., "A least-squares boundary residual method for numerical solution of scattering problems," *IEEE Transactions on Microwave Theory & Techniques*, Vol. 21, 99–104, 1973.
29. Bunch, K. J. and R. W. Grow, "The boundary residual method for three-dimensional homogeneous field problems with boundaries of arbitrary geometry," *International Journal of Infrared and Millimeter Waves*, Vol. 10, 1007–1032, 1989.
30. Sarkar, T. P., "A note on the variational method (Rayleigh-Ritz), Galerkin's method and the method of least squares," *Radio Science*, Vol. 18, 1207–1224, 1983.
31. Oraizi, H., "Application of least-squares method to electromagnetic engineering problems," *IEEE Antennas & Propagation Magazine*, Vol. 48, 50–74, 2006.
32. Mittra, R. and S. W. Lee, *Analytical Techniques in the Theory of Guided Waves*, MacMillan, New York, 1971.
33. Arizi, H. and R. Khalili, "Least-squares solution of junction of cylindrical waveguides of arbitrary cross-section," *International Journal of Engineering Science*, Vol. 12, 131–146, 2002.